measuring point 3m

# Modeling and simulation of a turbulent spray in urea-SNCR for biomass exhaust gas aftertreatment

Master's thesis in Sustainable Energy Systems

Oskar Finnerman

# Modeling and simulation of a turbulent spray in urea-SNCR for biomass exhaust gas aftertreatment

OSKAR FINNERMAN

Cover: Mass fraction profile for the DES the low temperature case. The location of a measuring point taken at the biomass boiler in Rörvik is also shown.

Modeling and simulation of a turbulent spray in urea-SNCR for biomass exhaust gas aftertreatment
OSKAR FINNERMAN
Department of Applied Mechanics
Chalmers University of Technology

# Abstract

The combustion of biomass is considered renewable since it is carbon neutral, but the combustion still releases nitrogen oxides ($NO_x$). Although not a greenhouse gas, the emission of $NO_x$ leads to acidification, eutrophication and smog. Therefore, it is interesting to evaluate techniques to remove $NO_x$ from biomass combustion. The technique looked into in this project is urea selective non-catalytic reduction(SNCR), where a spray consisting of urea and water is injected into the flue gas.

The aim of this project is to create a model for of the urea-SNCR process that can be used for design and optimization of the technique. Since the process is dependent on many complex phenomena such as turbulence, multiphase flow, chemical kinetics and mixing, a variety of models are evaluated with varying complexity. Three models are evaluated, both reactor models and computational fluid dynamics (CFD) models. The evaluated models are: reactor models - continuous stirred-tank reactor and continuous plug flow reactor, and turbulence models - k-$\epsilon$ and detached eddy simulation (DES). In order to determine the accuracy of the models, a comparison is made with measurement data from a biomass boiler located in Rörvik, Sweden. From the measurement data two operating temperatures are chosen, one over the optimal $NO_x$ reduction temperature and one below.

The results show that it is important to account for heat losses, and that there is a large difference between DES and k-$\epsilon$ for the higher temperature. This discrepancy is caused by the high sensitivity of the $NO_x$ reduction reaction to the reaction temperature. There are arguments for and against the use of DES instead of k-$\epsilon$, but more measurement data are needed in order to arrive at a definite conclusion.

Keywords: biomass combustion, $NO_x$ reduction, CFD, computational fluid dynamics, urea-SNCR, multiphase, DES, k-$\epsilon$

# Acknowledgements

I would like to thank Narges Razmjoo, Michael Strand and Jan Brandin at Linnaeus university, who have carried out the measurements used in this project. They have also provided insight into the geometry and behavior of the plant at Rörvik.

I would also like to thank Ning Guo, whom I worked with for a couple of months. Without his work, I would not have been able to carry out such extensive work which is presented in this report.

I give professor Srdjan Sasic my thanks for being my examiner.

Last but not least, I would like to thank my supervisor Henrik Ström. He has always been there to answer my questions in a thorough and pedagogical manner, which has made this project into an incredible journey in the world of CFD modeling.

<div align="right">

Oskar Finnerman, Gothenburg, September 2015

</div>

# Contents

# List of Figures

# List of Tables

# 1
# Introduction

## 1.1 Background

With an increased pressure from legislative authorities to decrease nitrogen oxides ($NO_x$) emissions due to environmental concerns, the incentives to decrease $NO_x$ emissions for industries are high [1]. The main negative effects on the environment are acidification, smog and eutrophication. $NO_x$ is also associated with effects on human health – it can cause irritation and swelling of the airways and is a big contributor of ground level ozone [2, 3].

Biomass as an energy carrier is considered renewable since it is carbon neutral, but the combustion of biomass still affects the environment negatively by releasing $NO_x$ [5]. It is therefore of great interest to reduce the $NO_x$ emissions of biomass combustion.

There are three main pathways causing formation of $NO_x$: fuel $NO_x$, which is caused by a reaction between oxygen in the air and nitrogen bounded in the fuel; thermal $NO_x$, which is formed at high temperatures by reactions between oxygen and nitrogen in the air; and prompt $NO_x$ which is created by nitrogen in the air and hydrocarbons from the fuel [4]. The largest contributor to $NO_x$ formation in the combustion of biomass is fuel $NO_x$ [5].

A number of techniques exist to combat $NO_x$ emissions; these include low-$NO_x$ burners, selective catalytic reduction (SCR) and selective non-catalytic reduction (SNCR). The technique modeled in this thesis is SNCR. In SNCR a reagent is injected into the flue gas where it reacts with $NO_x$ to form nitrogen and water. In this project the reagent is a urea-water solution which is used to treat the flue gas of a biomass boiler. The solution is injected into the flue gas stream where the droplets first will mix with the flue gas, this is followed by evaporation of water after which urea is decomposed into ammonia and lastly the ammonia reacts with the $NO_x$ in the flue gas to form nitrogen ($N_2$) and water ($H_2O$) [6].

The evaporation of water and subsequent reactions are dependent on many complex physical and chemical phenomena, consequently there are several ways to model the process and great care has to be taken when choosing models to describe the process.

## 1.2 Aim and scope

The aim of this Master thesis is to create a mathematical model of the urea-SNCR process that can be used for design and optimization. The description of the process

provided by the model will then be used to identify the strengths and areas of improvement of the urea-SNCR technique. The prediction of the behavior will be dependent on models used to describe the chemical kinetics, multiphase flow and turbulence. The interaction and impact of using different models are going to be investigated to identify effects that are left unresolved in typical simulation on an industrial scale that could increase accuracy of such simulations.

## 1.3   Framing of the problem

This thesis work aims to answer the following questions:

- What kinds of effects are left unresolved in a typical urea-SNCR simulation on industrial scale?
- Are the unresolved effects of any importance for the accuracy of the predicted $NO_x$ conversion?
- Is a more comprehensive model worth using considering computational time and accuracy of results?

## 1.4   Constraints and limitations

There are a series of limitations of this project, they are as follows:
- The simulations are restricted to the exhaust of the boiler, the furnace is not modeled.
- Biomass is the only fuel being considered.

# 2
# Theory

The theory necessary to understand the thesis work is presented below.

## 2.1 Urea SNCR process

In a urea-SNCR process a urea/water solution is injected into the flue gas stream where urea reacts with $NO_x$. The optimal temperature range is approximately between 900 °C and 1100 ° [6]. If the temperature is above this interval, the ammonia created from decomposition of urea will oxidize to NO. If the temperature is too low, the reaction rate will be slowed down which in turn leads to unreacted ammonia following the flue gas into the atmosphere. Great care has to be taken to ensure that temperature is kept in the right interval, since it is important to keep the $NO_x$ reduction as high as possible while ensuring low ammonia-slip. The steps that urea droplets goes through when they are injected into the flue-gas are illustrated in Figure 2.1.
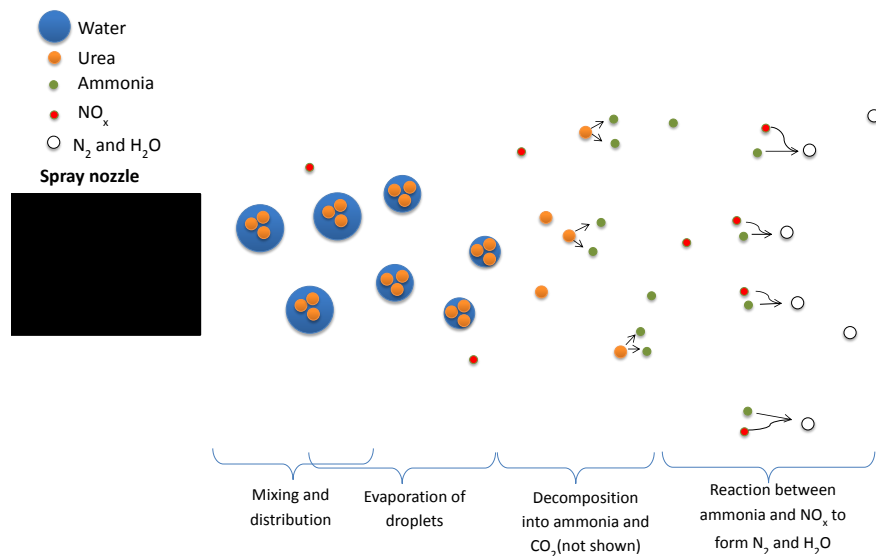


**Figure 2.1:** Illustration of the injected droplets

As seen in Figure 2.1, the droplets proceed through the following steps:

1. Mixing and distribution of the droplets in the flue gas.

2. Evaporation of water from the droplets.

3. Decomposition of urea into ammonia and carbon dioxide, which is the reducing agent.

4. Reaction between ammonia and $NO_x$ to form nitrogen ($N_2$) and water ($H_2O$). (There is also a competing reaction where ammonia oxidates into $NO_x$, which is not shown in the Figure 2.1) .

Not only temperature and mixing rate are important, but also droplet size. Before urea can decompose all of the water in the droplets must evaporate. This fact implies that the droplet size greatly influences the penetration depth of the spray, and as a consequence, where the reaction will occur. This behavior helps to increase the predictability of the process. The water in the urea spray can also help to cool the flue gas to desired reaction temperature if necessary [6].

### 2.1.1 Urea decomposition and breakdown

The thermal decomposition of urea is a complicated process with many different products and intermediates [7]. In this thesis the decomposition of urea ($NH_2CONH_2$) is simplified into the following two-step reaction proposed by Rota et al. [8], where $NH_3$ and isocyanic acid (HNCO) are formed:

$$NH_2CONH_2 \longrightarrow HNCO + NH_3 \tag{2.1}$$

$$HNCO + H_2O \longrightarrow NH_3 + CO_2 \tag{2.2}$$

The constants for the Arrhenius equation, Eq.2.3, describing the kinetics of the reactions are displayed in Table 2.1 where the units of A are in m-mol-s, and the units for E is in J/mol.

$$k = AT^b e^{E/RT} \tag{2.3}$$

**Table 2.1:** The Arrhenius constants for reaction 2.1 and 2.2

| reaction | A | b | E |
|----------|----------|---|-----------|
| 2.1 | 1.27E+04 | 0 | 65048.109 |
| 2.2 | 6.13E+04 | 0 | 87819.133 |

### 2.1.2 $NO_x$ reduction

The $NO_x$ reduction reaction is very complicated and a lot of research has been undertaken to understand the process better. The reduction of $NO_x$ consists of a large

number of elementary reactions steps, but there are simplified reaction schemes that can accurately describe this process. One of these schemes simplifies the reduction of $NO_x$ to just two reactions. This scheme was proposed by Ostberg et al. [9]:

$$NO + NH_3 + 0.25O_2 \longrightarrow N_2 + 1.5H_2O \tag{2.4}$$

$$NH_3 + 1.25O_2 \longrightarrow NO + 1.5H_2O \tag{2.5}$$
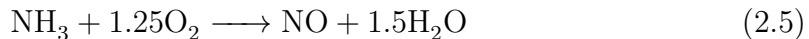
This simplified scheme is used in the project, where reaction 2.4 describes the reduction of NO while reaction 2.5 describes the oxidation of ammonia into $NO_x$. The reaction rate constants and orders of reaction used for this reaction were proposed by Brouwer et al. [10]:

$$R_{NO} = -k_r[NO][NH_3] + k_o x[NH_3][O_2] \tag{2.6}$$

$$R_{NH_3} = -k_r[NO][NH3] - k_{ox}[NH_3][O_2] \tag{2.7}$$

Where the $k$-constants are expressed in $m^3$/gmol,s and are defined as:

$$k_r = 4.24 \times 10^2 T^{5.30} e^{E_r/RT}; E_r = 349937.06 J/gmol \tag{2.8}$$

$$k_{ox} = 3.50 \times 10^{-1} T^{7.65} e^{E_{ox}/RT}; E_{ox} = 524487.005 J/gmol \tag{2.9}$$

## 2.2 Simulation models

In this subsection the models used to describe the many different physical phenomena related to this project are described.

### 2.2.1 Reactor models

Reactor models are, as the name implies, used to model chemical reactors. Mass and energy balances are made over the volumes in question after which ordinary differential equations can be constructed to describe the system. Below two ideal reactor models are introduced, the continuous stirred-tank reactor and the plug flow reactor models.

#### 2.2.1.1 Continuous stirred-tank reactor model

In the continuous stirred-tank reactor model (CSTR) the reactants are introduced into a perfectly mixed tank. Since it is perfectly mixed the whole reactor has the same temperature and concentration as the effluent.

The mole balance for the whole CSTR can be written as:

$$In - Out \pm Reactions = Accumulation \tag{2.10}$$

Since the reactor is continuous the accumulation term can be neglected. By approximating that the density is constant the molar balance can be expressed in concentrations, note that the units are in mol/s,

$$C_{in,i}q - C_{out,i}q \pm r_iV = 0 \tag{2.11}$$

$$C_{in,i} - C_{out,i} \pm r_i\tau = 0 \tag{2.12}$$

Where $C_i$ is the concentration of species $i$ given in mol/s, $q$ is the volume flow m$^3$/s, $V$ is the volume of the tank m$^3$, $r$ is the reaction term mole/m$^3$,s and $\tau$ is the retention time s. When the reaction is dependent on the different species concentrations it can be written as:

$$r_i = k_i \sum_{j=1}^{N} C_j^{\alpha_j} \tag{2.13}$$

Where $k$ is the reaction constant $N$ is the reactants (if the reactions are elementary), $\alpha_j$ is the stoichiometric constant and $C_j$ is the species concentrations influencing the reaction rate. Since the effluent has the same concentration as the tank, Eq. 2.12 can be rewritten as:

$$C_{in,i} - C_{out,i} \pm k_i\tau \sum_{j=1}^{N} C_{out,j}^{\alpha_j} = 0 \tag{2.14}$$

### 2.2.1.2 Continuous plug flow reactor model

The plug flow reactor (PFR) is often represented by a tubular reactor and it has two defining characteristics [11] :

1. There is no mixing in the direction of the flow, the reactants decrease in the direction of the flow and therefore the reaction rate $r_i$ also changes with the length of the reactor, and so does the temperature, depending on the heat of reaction.

2. There is no radial variation of concentrations or temperature, therefore the variations are only in the flow direction. This implies that the PFR is a 1D model.

The derivation of the ordinary differential equation (ODE) describing the PFR starts with a mass balance over the control volume shown below in Figure 2.2.
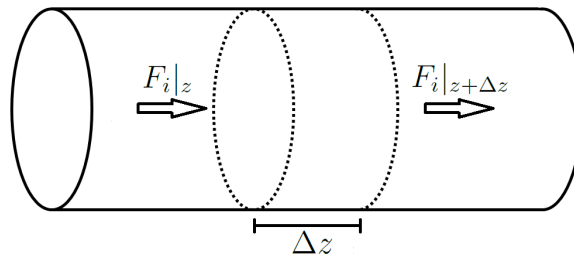


**Figure 2.2:** Control volume of a plug flow reactor

$$In - Out \pm Reaction = Accumulation \tag{2.15}$$

Writing the terms and setting the accumulation term equal to zero,

$$F_i|_z - F_i|_{z+\Delta z} \pm r_i \Delta z * A = 0 \tag{2.16}$$

Dividing with z and letting z $\rightarrow$ 0,

$$\frac{dF_i}{dz} \pm r_i A = 0 \tag{2.17}$$

Re-arranging the terms and writing the expression for r as dependent on concentration,

$$dF_i \pm k_i C_j A dz = 0 \tag{2.18}$$

Expressing the convection as molar concentration,

$$dC_i \pm k_i C_j d\tau = 0 \tag{2.19}$$

Where $d\tau$ and $C_j$ is the retention time and concentration $j$ respectively for length $dz$. To solve this equation, it needs to be integrated over the whole reactor length.

As the equations imply, the tube and the tank reactors will behave differently. The production term in the CSTR is constant while the production term in the PFR will change with the length of the reactor. Depending on the order of the reaction, the final concentrations of the reactants between the CSTR and PFR may be different. For a first order reaction the PFR will have lower reactant concentration at the outlet. This behavior is because the concentration of the reactants are higher on average, which leads to higher reaction rate since $r$ is proportional to $C_i$. Other factors, such as exothermic/endothermic reactions, will also affect differences in concentration profiles for PFRs and CSTRs.

When deciding whether to use the CSTR or PFR model to describe a process it is important to know the geometry of the domain and properties of the flow, often the real process behaves like a combination of the two reactor models.

### 2.2.2 Turbulence models

Turbulence are chaotic seemingly random flows that consists of small scale and high-frequency fluctuations. Therefore a lot of information is required to fully describe this phenomenon. Thankfully, the amount of information can be substantially decreased by manipulating the Navier-Stokes equations to remove small scale fluctuations. Such manipulation will require modeling of the small scale fluctuations in order to describe them. The fluctuations can be removed to varying degrees, from the Reynolds Averaged Navier-Stokes equations where the mean variables are calculated while the fluctuating variables are modeled, to applying filtering functions where everything but the smallest scales are calculated directly. Increased resolution requires smaller steps in time and space, which will result in more computation time. That is why it is often desirable to filter out as many small scale fluctuations as possible that the specific case allows. The different turbulent models used in this thesis are described below.

### 2.2.2.1   k-$\epsilon$ model

The k-$\epsilon$ model describes the fluctuating properties in the Reynolds-averaged Navier-Stokes equations (RANS equations). These equations are derived from the Navier-Stokes equations by decomposing the quantities into one time averaged and fluctuating property, see the equations below where this is done for the velocity.

The continuity equation for incompressible flow

$$\frac{\partial U_j}{\partial x_j} = 0 \tag{2.20}$$

The Navier-Stokes equations

$$\frac{\partial U_i}{\partial t} + U_j \frac{\partial U_i}{\partial x_j} = -\frac{1}{\rho} \frac{\partial P}{\partial x_i} + \nu \frac{\partial^2 U_i}{\partial x_j \partial x_j} \tag{2.21}$$

Decomposing velocity into one time-averaged and one fluctuating part.

$$U_i = \bar{U}_i + u_i \tag{2.22}$$

By inserting Eq. 2.22 into the continuity equation (2.20) and the Navier Stokes equations (2.21) we obtain the time-averaged equations.

$$\frac{\partial \bar{U}_j}{\partial x_j} = 0 \tag{2.23}$$

$$\frac{\partial \bar{U}_i}{\partial t} + \bar{U}_j \frac{\partial \bar{U}_i}{\partial x_j} = -\frac{1}{\rho} \frac{\partial \bar{P}}{\partial x_i} + \nu \frac{\partial^2 \bar{U}_i}{\partial x_j \partial x_j} - \frac{\partial \overline{u_i u_j}}{\partial x_j} \tag{2.24}$$

Where the last term is called the Reynolds stress tensor. It represents a correlation between fluctuating velocities and must be modeled in order to close the equation system. This is where the k-$\epsilon$ model comes into play.

The k-$\epsilon$ model is used to model the Reynolds stress tensor. The modeling is made possible by making the Boussinesq assumption, that the Reynolds stress is proportional to the mean velocity gradients times the turbulent viscosity. Turbulent viscosity is analogous to molecular viscosity in such way that it is used to describe momentum transfer caused by turbulent eddies, like molecular viscosity is used to describe momentum transfer by molecular diffusion. The Boussinesq assumption is written as:

$$-\overline{u_i u_j} = \nu_T \left( \frac{\partial \bar{U}_i}{\partial x_j} + \frac{\partial \bar{U}_j}{\partial x_i} \right) - \frac{2}{3} k \delta_{ij} \tag{2.25}$$

Where $\delta_{ij}$ is the Kronecker delta which is 1 for $i = j$ and 0 for $i \neq j$, and $k$ is the turbulent kinetic energy. Assuming incompressible flow, the modeled transport equation for k can be written as,

$$\frac{\partial k}{\partial t} + \bar{U}_j \frac{\partial k}{\partial x_j} = \frac{\partial}{\partial x_j} \left[ \left( \nu + \frac{\nu_T}{\sigma_k} \right) \frac{\partial k}{\partial x_j} \right] + P_k - \nu \overline{\left( \frac{\partial u}{\partial x_j} \frac{\partial u_i}{\partial x_j} \right)} \tag{2.26}$$

Where $\nu_T$ is turbulent viscosity, $\sigma_k$ is the turbulent Prandtl number for $k$ and $P_k$ is the production term. The last term on the right hand side is dissipation of $k$ by viscous stresses, where the kinetic energy of the turbulence is transformed into heat. This term also needs to be modeled in order to close the equation system. In k-$\epsilon$ it is modeled by the transport equation for turbulent dissipation $\epsilon$, which is seen below in Eq. 2.27,

$$\frac{\partial \epsilon}{\partial t} + \bar{U}_j \frac{\partial \epsilon}{\partial x_j} = \frac{\partial}{\partial x_j} \left[ \left( \nu + \frac{\nu_T}{\sigma_\epsilon} \right) \frac{\partial \epsilon}{\partial x_j} \right] + P_k C_{1\epsilon} \frac{\epsilon}{k} - C_{2\epsilon} \frac{\epsilon^2}{k} \qquad (2.27)$$

Where C$_{1\epsilon}$, C$_{2\epsilon}$ are constants and $\sigma_\epsilon$ is the turbulent Prandtl number for $\epsilon$.

The k-$\epsilon$ model is a stable model and therefore used in many engineering applications. Its popularity is due to the the straightforward modeling of the dissipation, since it appears directly in the equation for turbulence. The k-$\epsilon$ model is a good compromise between generality and required CPU-power for many industrial CFD-problems [12]. It is therefore a natural choice in this project and will serve as an excellent comparison to the other models tested in this thesis.

**2.2.2.1.1 Wall functions**  The standard $k - \epsilon$ model and its constants are developed for fully turbulent flow, further $k$ and $\epsilon$ does not go to zero at correct rate at the wall (see further discussion in 2.2.2.2 k-omega model). It is therefore necessary to use wall functions to model the behavior of the fluid closest to the walls. The standard wall function for the k-$\epsilon$ model can be seen below in Eq.2.28,

$$\bar{U}_x = \frac{1}{\kappa} ln(y^+) + B \qquad (2.28)$$

Where $\kappa$ is the von Karman constant which is set to 0.42 and $B = 5.0$, and $y^+$ is the dimensionless wall distance. These dimensionless properties enables the function to be used on general problems.

The wall functions are used in the cells closest to the boundary and it is important that these cells are of the right size: if they are too small the turbulence models will be used on parts of the flow near the boundary where the wall functions are optimally used, if the cells are to large the wall functions will be used in flow regions that they are not designed for. $y+$ is often used to describe the optimal distance from the wall, and the $y+$ values should be typically between 20 and 30. The upper limit is usually in the range of 80-100 [12].

Wall functions can also be used on other turbulence models, and it is even sometimes used on models which can predict accurate behavior at the boundaries. In these occasions it is used as a very effective tool to decrease the required density of the mesh at the boundaries, by simply using wall functions closest to the boundary, see Figure 2.3.
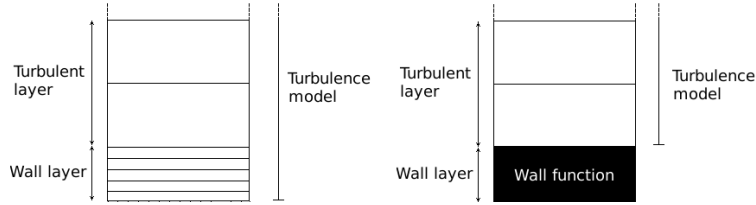
**Figure 2.3:** Cells with and without wall functions at the boundary

#### 2.2.2.2 k-$\omega$ model

Another way to model the dissipation term in the transport equation for $k$ is to use $\omega$ instead, this quantity is called specific dissipation and it is proportional to $\epsilon/k$. The $k - \omega$ model was originally suggested by Wilcox [13], and it is his suggested model [14] that the standard k - $\omega$ model in the commercial CFD software ANSYS FLUENT is based on [15], which is displayed in equations Eq. 2.29 - 2.30 below. Note that the $k$ equation has been modified to enable the dissipation to be expressed in terms of $\omega$, which has the unit $t^{-1}$.

$$\frac{\partial k}{\partial t} + \bar{U}_j \frac{\partial k}{\partial x_j} = \frac{\partial}{\partial x_j}\left[\left(\nu + \frac{\nu_T}{\sigma_k^w}\right)\frac{\partial k}{\partial x_j}\right] + P_k - \beta^* k \omega \tag{2.29}$$

$$\frac{\partial \omega}{\partial t} + \bar{U}_j \frac{\partial \omega}{\partial x_j} = \frac{\partial}{\partial x_j}\left[\left(\nu + \frac{\nu_T}{\sigma_\omega}\right)\frac{\partial \omega}{\partial x_j}\right] + c_{\omega 1}\frac{\omega}{k}\nu_T P_k - c_{\omega 2}\omega^2 \tag{2.30}$$

Where $\beta^*$, $c_{\omega 1}$, $c_{\omega 2}$, $\sigma_\omega$ and $\sigma_k^w$ are constants.

The $k - \omega$ model is better at handling flows with low turbulence compared to $k - \epsilon$. This is because $k$ and $\epsilon$ are unable to approach zero at the correct rate when the turbulence decreases due to numerical problems in the expression for dissipation. The $\epsilon$ equation contains the expression $\frac{\epsilon^2}{k}$ which is $\mathcal{O} = y^{-2}$, and therefore tends to infinity when the turbulence is decreased. No such problem exists for the $k - \omega$ model because $\omega$ is $\mathcal{O} = y^0$ which simply goes to zero as the turbulence decreases. Thus, the $k - \omega$ model is better at predicting boundary flows, where the turbulence of naturally goes to zero. It is therefore possible to use $k - \omega$ without wall functions, which is required when using the standard $k - \epsilon$ model. Using the turbulence model all the way to the wall will however require a very fine grid at wall region. When using the standard $k - \omega$ model in FLUENT, the wall functions are used where the grid is too coarse for an accurate prediction of the flow, and omitted where the grid is fine enough [16].

A popular version of the $k - \omega$ model is the SST $k - \omega$ model proposed by Menter [17]. It is a hybrid version between $k - \epsilon$ and $k - \omega$. The $k - \omega$ model is used in regions with low Reynolds number and $k - \epsilon$ is used in the free stream since the $k - \omega$ model is sensitive to inlet turbulent properties.

#### 2.2.2.3 LES

In Large Eddy simulation (LES) a spatial filtering equation is applied to the Navier-Stokes equations to filter out the smallest eddies. The large eddies are calculated

directly while the smaller scales are modeled using sub-grid models. A variable space filter is applied on the Navier-Stokes equation for velocity $U_i$ below,

$$\bar{U}_i(x) = \iiint U_i(x')G(x,x')dx \tag{2.31}$$

Where G is a filter function which is zero for values of $U_i$ occurring at small scales. Filtering the Navier-stokes equation 2.21 gives the filtered Navier-Stokes equation,

$$\frac{\partial \bar{U}_i}{\partial t} + \bar{U}_j\frac{\partial \bar{U}_i}{\partial x_j} = -\frac{1}{\rho}\frac{\partial \bar{P}}{\partial x_i} + \nu\frac{\partial^2 \bar{U}_i}{\partial x_j \partial x_j} - \frac{\partial \tau_{ij}}{\partial x_j} \tag{2.32}$$

It looks quite similar to the RANS-equation 2.24 but with the difference that the Reynolds stress tensor is replaced by the the residual stress tensor $\tau_{ij}$ which needs to be modeled using sub-grid models, such as Smagorinsky-Lilly [18] or WALE [19]. It is desired that the filter resolves at least 80 % of the eddies. This requirement is due to the anisotropic behavior of the larger eddies and the history effects they are subjected to, which are hard to model. It is therefore best to solve for these eddies directly. The smaller eddies are more fitting to be modeled since they can be regarded as largely isotropic and are not as dependent on history effects. If a filter is used that removes larger eddies the accuracy might decrease since the calculation becomes more dependent on the modeling of residual scales [12].

The advantages of using LES compared to RANS-models is the increased accuracy obtained when larger eddies are resolved directly. But resolving the larger eddies requires LES to be transient, that and the requirement of having a small grid together with satisfyingly small time steps, leads to the greatest drawback compared to RANS - the increased computational cost.

**2.2.2.3.1   Grid size**   The size of the cells will decide the resolution of the LES-simulation if the mesh is used as the filter, like it is in this project. The cells should be sufficiently small to resolve the smallest eddies intended to be calculated directly. At least a couple of cells are needed per integral length scale in order to properly resolve the smallest eddies intended to be resolved.

**2.2.2.3.2   Time step**   The time step must be small enough to provide an adequate temporal resolution when a fluid element passes through a cell. To approximate the necessary time step, the cell length is divided with the local velocity, which gives the time that the fluid element spends in the cell,

$$\Delta t = \frac{\Delta x}{U} \tag{2.33}$$

The fraction of the cell length and the product of velocity and the time step is called the Courant number, see Eq.2.34, it is a meassure of time resolution and should be <1 for explicit schemes in order for the solver to be stable. For implicit schemes the requirement on the Courant number is not as strict numerically, since it is unconditionally stable. It is however preferable not to have it <1, in order to obtain sufficient time resolution in LES [20].

$$\text{Courant number} = \frac{U\Delta t}{\Delta x} \tag{2.34}$$

**2.2.2.3.3 LES inlet conditions** It is important to specify a realistic turbulent inflow velocity to accurately predict the downstream flow. To achieve this, perturbations are created at the inlet that generates local imbalances in the velocity field creating instant velocity components which will "trigger" the unsteady velocity fluctuations associated with turbulence. One way to trigger these perturbations is with the the spectral synthesizer method suggested by Kraichnan [21] and modified by Smirnov et al. [22]. It utilizes random Fourier modes that creates a turbulent velocity field.

Since the inlet conditions are artificial, the region of interest need to be sufficiently far downstream so the flow field is adjusted to the rest of the domain rather than being influenced by the arbitrary conditions imposed at the inlet.

**2.2.2.3.4 LES initial conditions** Perturbations can be initialized in the whole domain to further contribute to the creation of instant velocity components. These perturbations can also be created with the spectral synthesizer, which superimposes turbulence on top of the mean velocity field.

### 2.2.2.4 DES

Detached Eddy Simulation (DES) is a turbulence model that uses RANS at the boundaries and LES at the other regions. It couples the benefits of RANS and LES while minimizing their disadvantages. It combines the accuracy of predicting attached boundary layers from RANS with the ability to capture unsteady motions of large eddies by LES. The model is also more economical in terms of computational costs compared to pure LES - the resolution at the boundary layers for LES needs to be sufficiently fine to resolve the small eddies there, but when using RANS at the boundaries the grid can be much coarser and therefore saving CPU-time.

Different RANS-models can be used to simulate the boundaries in DES, the one used in this project is the SST $k - \omega$ model. In FLUENT the dissipation term in the equation for $k$ (Eq. 2.26) is modified for the DES-model as described by Menter [23] so that [24]:

$$\nu \overline{\left( \frac{\partial u}{\partial x_j} \frac{\partial u_i}{\partial x_j} \right)} = \rho \beta^* k \omega F_{DES} \tag{2.35}$$

Where $F_{DES}$:

$$F_{DES} = max \left( \frac{L_t}{C_{DES}\Delta_{max}}, 1 \right) \tag{2.36}$$

Where $C_{DES}$ is a calibration constant which has a value of 0.61, $\Delta_{max}$ is the maximum local grid spacing and $L_t$ is the turbulent length scale is the parameter that defines this RANS model, which is expressed as:

$$L_t = \frac{\sqrt{k}}{\beta^*\omega} \tag{2.37}$$

### 2.2.3 Energy transport

Energy is present in many forms, such as kinetic energy of the flow, bounded energy in chemical bounds, and thermal energy. To account for energy transport in modeling of transport phenomena, balance equations are made. The balance equation for total energy is shown below [12],

$$\frac{\partial h}{\partial t} = -\frac{\partial}{\partial x_j}\left[hU_j - k_{eff}\frac{\partial T}{\partial x_j} + \sum_n m_n h_n\right] + S_h \qquad (2.38)$$

where $h$ is the total enthalpy in J/m$^3$, $k_{eff}$ is the effective constant for thermal conductivity and $h_n$ is the heat of reaction and $S_h$ is an external heat source term. Note that the terms describing diffusion and dissipation of heat are excluded from the equation above, since the effects of these terms are neglected in the simulations.

In the CFD-simulations the energy equations will be solved in conjunction with the turbulence models.

#### 2.2.3.1 Boundary conditions for energy equations

The inlet and outlet boundary conditions for energy equations are similar to boundary conditions for momentum. The wall boundary conditions can however be quite different. The walls can be adiabatic, have a constant temperature or transfer heat trough convection or radiation. In this thesis the walls are going to be adiabatic or transfer heat trough convection.

### 2.2.4 Turbulence-chemistry interaction models

When modeling reactive flows in CFD the first thing to consider is whether the mixing rate or the reaction rate is the rate-determining step in the overall reactions. This question can be answered by calculating the Dahmköhler number,

$$Da = \frac{\text{Typical time required for mixing}}{\text{Typical time required for chemical reaction}} \qquad (2.39)$$

The typical time required for a reaction can be estimated as the time required for a complete consumption of the limiting reactant assuming constant reaction rate at present reactions. The typical time required for mixing in a turbulent flow can be determined by [12],

$$\tau_{mixing} = \sigma\frac{k}{\epsilon} \qquad (2.40)$$

Where $\sigma$ is a constant commonly set to 0.5.

If the Dahmköhler number is much smaller than unity, the chemical reaction rate can be regarded as the rate-determining step. The cells will therefore have homogeneous mixture before any chemical reactions takes place, and the overall rate of the reaction in each cell is calculated only by the Arrhenius equations Eq.2.3 for the corresponding reactions.

If the Dahmköhler number is much larger than unity, the mixing rate is the rate-determining step for the overall reaction. It implies that the reactants are not

perfectly mixed in the cells before the reactions takes place. The eddy-dissipation model developed by Magnussen and Hjertager [25] Eq.2.41-2.42 can be used to calculate the overall reaction rate in these circumstances. The model calculates the reaction rate based on large-eddy mixing time-scale $k/\epsilon$. The net rate of production of species $i$, caused by reaction $r$ has the reaction rate $R_{i,r}$, which is given by the smallest value of the expressions below:

$$R_{i,r} = \nu'_{i,r} M_{w,i} A \rho \frac{\epsilon}{k} min_R \left( \frac{Y_R}{\nu'_{R,r} M_{w,R}} \right) \tag{2.41}$$

$$R_{i,r} = \nu'_{i,r} M_{w,i} A B \rho \frac{\epsilon}{k} min_R \left( \frac{\sum_p Y_R}{\sum_j^N \nu''_{R,r} M_{w,j}} \right) \tag{2.42}$$

Where $Y_p$ is the mass fraction of product species $P$, $Y_R$ is the mass fraction of a particular reactant $R$, and $A$ and $B$ are empirically determined constants set to 4.0 and 0.5 respectively. As anticipated, smaller mixing time scale (inverse of $\epsilon/k$) leads to higher reaction rate.

If the Dahmköhler number is approximately 1, both the mixing rate and the chemical reaction rate are of the same order of magnitude. In this case the overall reaction rate can be estimated by calculating both the reaction rate by eddy dissipation and Arrhenius equation and letting the lowest reaction rate determine the overall reaction rate.

### 2.2.5 Multiphase models

Multiphase flows are common in the nature as well as in industrial applications. They are therefore an important concept to master when trying to understand the fluid phenomena around us. Examples of multiphase flows in industrial applications are: steam bubbles created in boiling processes, the bed material flow in a fluidized bed and the injection of fuel into combustion engines. Multiphase flows are classified according to the state of matter included in the flow and whether the flow is separated or dispersed.

The turbulent spray modeled in this thesis is an example of a dispersed multiphase flow, since the droplets have individual interfaces with the continuous phase.

Like in many other fluid flow phenomena, a multiphase flow can be characterized by dimensionless numbers. One is the volume fraction which is seen below in Eq. 2.43 which determines how much of the total volume is occupied by the dispersed phase.

$$\alpha_d = \frac{\sum_{i=1}^{N_d} V^i}{V} \tag{2.43}$$

It can be used to determine the typical distance between particles in Eq. 2.44. It is an important factor when determining inter-particle interactions.

$$L = D_d \left( \frac{\pi}{6\alpha_d} \right)^{1/3} \tag{2.44}$$

Time and length scales are also important in the characterization of multiphase flows, like it is for turbulent flows. For multiphase flows, these scales can be used

to describe the inertia of the dispersed phase and the continuous phase, collisions between particles or droplets, or diffusion of the dispersed phase caused by turbulence.

All these phenomena are described by different dimensionless Stokes numbers wherein time scales are compared. One example is the turbulent Stokes number which is used to describe the ratio of inertia between the dispersed and the continuous phase(see Eq. 2.45).

$$St_T = \frac{\tau_d}{\tau_T} \tag{2.45}$$

Where $\tau_d$ is the timescale of the dispersed phase and $\tau_T$ is the timescale of the turbulence which can be obtained from $k/\epsilon$. The particle response time can be obtained from Eq. 2.46

$$\tau_d = \frac{\rho_p d_p^2}{18\mu} \frac{24}{C_D Re} \tag{2.46}$$

Where $\rho_p$ is the particle density, $\mu$ is the molecular viscosity of the continuous phase, $d_p$ is the particle diameter, $Re$ is the particle Reynolds number and $C_D$ is the drag coefficient. In the expression for the drag coefficient below, it is assumed that the particles are smooth spheres,

$$C_D = a_1 + a_2/Re + a_3/Re^2 \tag{2.47}$$

Where $a_1$, $a_2$ and $a_3$ are constants given by given by [26] that apply over several ranges of Re.

When $St_\tau \Rightarrow 0$ the particle will follow the flow completely and for flow where $St_\tau \Rightarrow \infty$, the inertia of the particle will be so large that its flow path is not affected by the flow of the continuous phase.

Hitherto only the influence of the continuous flow on the dispersed phase has been discussed, but it is also important to consider the opposite. To determine if the particles have any impact on the continuous flow the Stokes numbers and the volume fraction of the dispersed phase need to be evaluated. If the Stokes number is larger than unity and if the volume fraction of the dispersed phase is large enough to have an impact on the average density of the mixture, coupling between the continuous phase and the dispersed phase has to be considered. The coupling is naturally not only limited to the exchange of momentum, but also the exchange of heat and mass. Heat exchange appears as a heat source or sink in the energy equation for the continuous phase. While mass exchange appears as a mass source or mass sink in the continuity equation, and as a source or sink of chemical species in the species transport equations.

If the volume fraction is increased even further particle-particle interactions also need to be considered. Increased coupling between the dispersed phase, continuous phase and particles increases the complexity of the model.

As the discussion above implies, there exist many phenomena and physical circumstances that have to be taken into account when modeling multiphase flows. Understandably, it therefore exists many models to predict them, and choosing the

most suitable one depend, among others things, on the physical properties described above. The models used in this thesis are described below.

### 2.2.5.1 Lagrangian particle simulation

The Lagrangian particle simulation can be used on systems with low volume fraction of dispersed particles and where it is reasonable that the dispersed phase influences the continuous phase and vice versa. The particles are tracked individually while the fluid phase is modeled as a continuum by solving the Navier-Stokes equations. To save computational power, the particles can be grouped together into bundles where it is assumed that all particles within the bundle has the same properties as the center of gravity for the particles [12].

The influence of the particles on the continuum is taken into account by adding source terms to the Navier-Stokes equation of the fluid seen below in Eq.2.48-2.49. They are solved in conjunction with tracking the individual particles.

$$\frac{\partial(\alpha_f \rho_f)}{\partial t} + \frac{\partial(\alpha_f \rho_f U_{i,f})}{\partial x_i} = S_c \tag{2.48}$$

$$\frac{\partial(\alpha_f \rho_f)}{\partial t} + U_{i,f}\frac{\partial(\alpha_f \rho_f U_{i,f})}{\partial x_i} = \alpha_f \frac{\partial P}{\partial x_i} + \frac{\partial(\alpha_f \tau_{ij,f})}{\partial x_j} + S_{i,j} \tag{2.49}$$

Where $Sc$ is a source term that describes mas transfer between the phases and $S_{i,p}$ describes the momentum exchange between the particles and the fluid. However, in the simulations carried out in this project the contribution from $Sc$ is neglected. To be able to asses the impact of the particles in the source term describing the momentum exchange, and to calculate the motion of the particle fluctuations, a force balance must be made over the particles.

$$m_p \frac{d\boldsymbol{u}_{i,p}}{dt} = \sum_{\boldsymbol{x}} \boldsymbol{F_x} \tag{2.50}$$

Where $\boldsymbol{u}_{i,p}$ is the linear velocity of the particle and $\sum_{\boldsymbol{x}} \boldsymbol{F_x}$ is the sum of all forces acting on the particle. Some of the forces that are usually included are shown below [27]:

- Drag force, which is the relative velocity between particle and the fluid surrounding it.
- Buoyancy force caused by gravitation.
- Virtual mass forces, which is due to acceleration of the surrounding fluid.
- History forces, due to changes of the continuous phase boundary layer.
- Brownian motions, caused by collisions of molecules.
- Lift force, due to velocity gradients normal to the flow.
- Rotational force, caused by rotation of the particle.
- Thermophoretic force which is cased by temperature gradients over the droplet.

In this thesis all forces except drag force are neglected for the sake of simplicity, and because it has been determined that the effects of several of the forces are comparatively small for a urea-spray simulation in similar operating conditions [27]. In FLUENT the drag force is in turn calculated by [28],

$$F_{drag} = \boldsymbol{u} - \boldsymbol{u_p}/\tau_r \tag{2.51}$$

Where $\boldsymbol{u}$ is the fluid phase velocity, $\boldsymbol{u_p}$ is the particle velocity and $\tau_r$ is the particle relaxation term, it is calculated by Eq. 2.46.

The particles have to be much smaller than the grid cells, because the velocity field of the continuum used to calculate the source terms have to be unaffected by the particles [12]. The movement of the particles are calculated by integrating their trajectory Eq.2.52 and the force balance over the particles Eq.2.50.

$$\frac{dx_i}{dt} = u_{i,d} \tag{2.52}$$

### 2.2.5.2   Discrete random walk model

The effects of the turbulence of the particles depend on the Stokes number. If the Stokes number is small enough the turbulent eddies will move the particles in random directions other than the average paths. The discrete random walk model can be used to simulate this behavior by adding a random velocity to the continuous phase for a time $T$, which is the time a particle spends in an eddy. This time is the minimum estimate of the time it takes for a particle to pass through an eddy and the lifetime of the turbulent eddy. The time taken to pass through the eddy can be expressed as a function of the size of the turbulent eddy and the slip velocity, see Eq. 2.53

$$T \approx -\tau ln \left( 1 - \frac{l}{\tau |U_d - \bar{U}_f|} \right) \tag{2.53}$$

Where $\tau$ is the particle response time, see Eq.2.46, and $l$ is the size of the turbulent eddy. The lifetime of a turbulent eddy in RANS is proportional to $k/\epsilon$.

The random turbulent velocity fluctuation is assumed to have Gaussian probability distribution, the expression for the fluctuating velocity component is shown in 2.54

$$u_i^{'} = \xi_i\sqrt{\bar{u_i^2}} \tag{2.54}$$

Where $\xi$ is a random Gaussian number.

For isotropic turbulence $\bar{u_1^2} = \bar{u_2^2} = \bar{u_3^2} = 2/3k$, which makes it possible to express 2.54 as follows:

$$u_i^{'} = \xi_i\sqrt{2/3k} \tag{2.55}$$

$k$ is known from the transport equations for turbulence, which enables the random fluctuating velocity $u_i^{'}$ can be calculated. This velocity is added to the average velocity of the continuum and kept constant during the time $T$. A new random

Gaussian number $\xi$ is chosen after each time-step, which over time will create a random distribution of particles in the flow.

### 2.2.5.3   Droplet heat and mass transfer

As described by Henrik et al. [27] the continuous and discrete phase for the urea-SNCR process can be modeled as two-way coupled in regard to the heat and mass transfer between the phases. The droplets are assumed to be homogeneous, therefore no internal transport takes place inside the droplets. As previously described, the water in the droplets will evaporate until there is only urea left. When the urea has melted the urea will start to thermally decompose, it is modeled as a evaporation process as described by Lundström et al. [29]. The melting of urea is not modeled but the enthalpy of fusion is accounted for when calculating the urea vapor pressure.

# 3

# Methodology and case specifications

The simulation process for the different cases are to be presented here. An overview of the biomass boiler in Rörvik is also going to be given, which was where measurement data was obtained from.

## 3.1 The biomass boiler in Rörvik - geometry and measurement data

Measurement data was obtained from a commercial biomass boiler located in Rörvik, Sweden. The measurements are obtained for a boiler loading of 3 MW.

### 3.1.1 Geometry of Rörvik

A simplified schematic of the geometry of the boiler is shown below in Figure 3.1. The exhaust part, which is to be modeled, is marked in red.
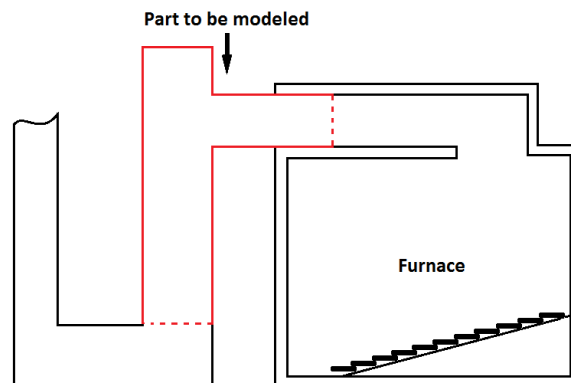


**Figure 3.1:** Simplified schematic of the boiler.

A detailed schematic of the exhaust part is provided below in Figure 3.2. The location of the urea injector is shown in the schematic, it is inserted 20 cm from the side-wall at 0.57 meters upstream from the intersection of the two pipes.
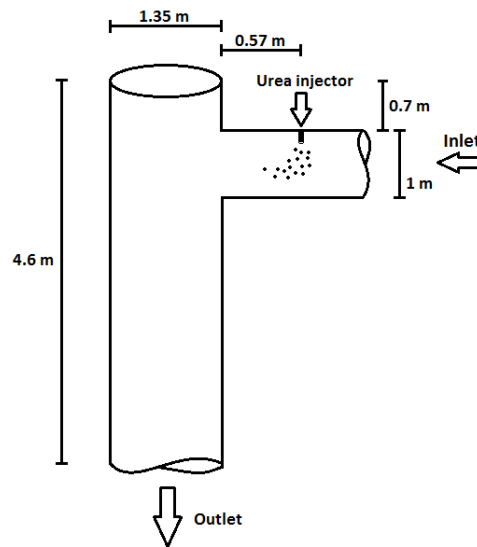
**Figure 3.2:** Schematic of the exhaust part, with a visualization of the placement of the urea injector.

It is seen that the geometry consists of two pipes that intersect each other. The pipe that receives the inlet flow is from now on referred to as "inlet pipe" and the other pipe is referred to "outlet pipe". The whole domain is simply referred to as "the domain", "exhaust pipe" or "exhaust part" when it is to be distinguished from the rest of the furnace. From this schematic, the geometry for the simulation was created in the Design Modeler program in ANSYS FLUENT. The resulting geometry is provided below in Figure 3.3. The inlet of the inlet pipe is placed 5 diameters upstream from the injector, in order make sure that the synthetic perturbations created at the inlet of the DES-simulations does not influence the critical parts of the domain, which are downstream of the spray. This geometry is also used in the k-$\epsilon$ models.
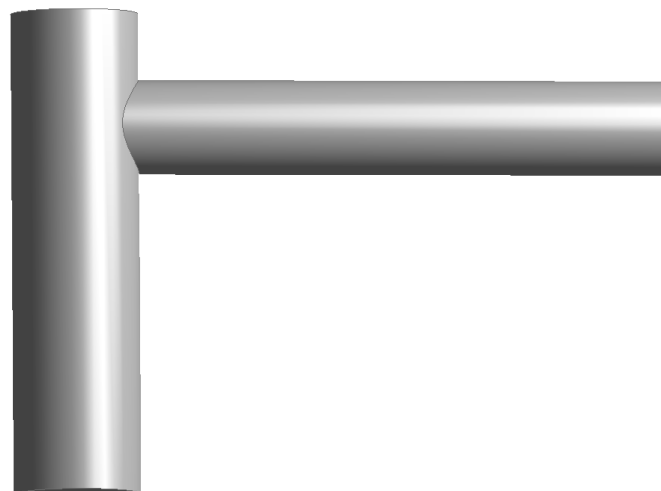


**Figure 3.3:** Schematic of simulation geometry.

### 3.1.2 Measurement data from Rörvik

Two operating temperatures were chosen from the collection of data, one higher and one lower temperature. The measurements were taken by a probe on the end of a lance that was inserted from the top of the exhaust pipe. Measurements were taken at three locations: at 1 meter, 2 meters and 3 meters below the top of the pipe, most of them both with and without the urea injection turned on. The measurements are averaged over time, but due to the nature of the measuring technique the exact positioning of the probe in the plane perpendicular to the lance is uncertain. It is therefore assumed that the probe is measuring at the center of the pipe, since that is the most likely position. A schematic of the placement of the lance and the position of the measurement locations are shown below in Figure 3.4.
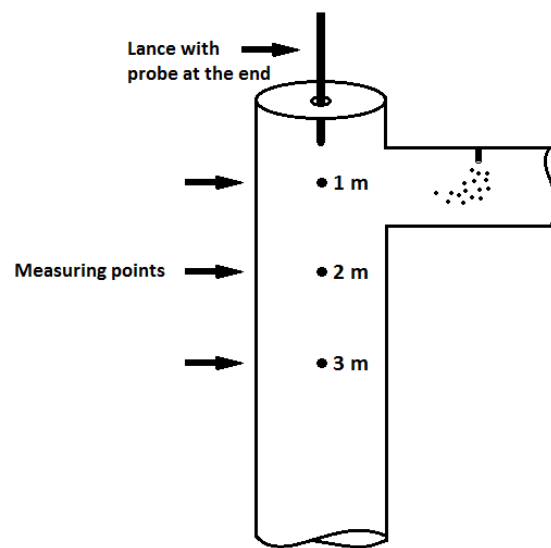


**Figure 3.4:** Schematic of the lance and measuring points.

Three factors regarding the measurement data were especially important to take into consideration when implementing them in the models: 1) No measurements were taken in the inlet pipe; 2) The exhaust pipe appeared to have heat losses to the surroundings, since the measured temperature decreased as the lance was moved downwards from the top of the exhaust pipe; 3) No measurements were taken at 1 meter when the urea was turned off for the lower operating temperature.

Since there was no temperature data for the inlet pipe, it was assumed to be adiabatic.

To obtain inlet data for the higher temperature case, the temperature and species data at the inlet were assumed to be the same as the data at 1 meter when the urea injection was turned off. To take the heat loss into account a heat transfer coefficient was calculated by iterating the heat transfer coefficient in k-$\epsilon$ simulations for a known temperature at 1 meter, until the calculated temperature at 3 meters was the same as the measurement data. A block scheme of this procedure to obtain the heat transfer coefficient is shown below in Figure 3.5.
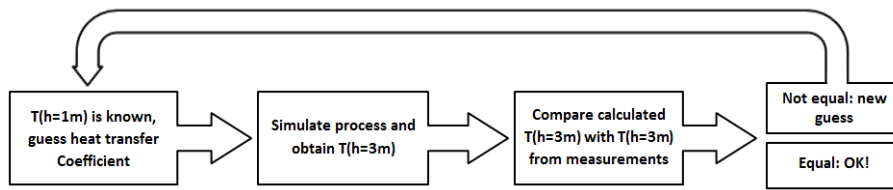
**Figure 3.5:** Block scheme of calculations to obtain the heat transfer coefficient.

Since there was no measuring data at 1 meter for the low temperature case, the data for the species concentrations were obtained from 3 meters below the top of the exhaust pipe when urea was turned off. The inlet temperature was obtained by assuming the same heat coefficient as in the high temperature case and then iterating the inlet temperature until the temperature at 3 meters was the same as in the data. A block scheme depicting the calculations to obtain the inlet temperature of the low-temperature case is presented below in Figure 3.6.
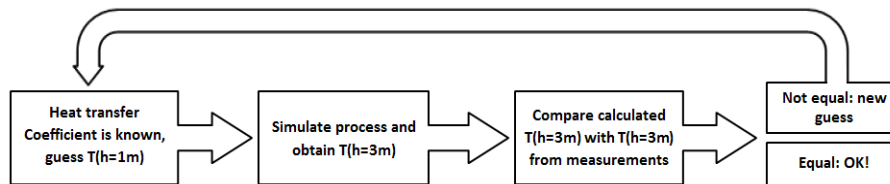


**Figure 3.6:** Block scheme of calculations to obtain the outlet temperature for the case with low operating temperature.

The inlet temperatures were calculated to 1115 $K$ for the low temperature case and 1238.8 $K$ for the high temperature case. The heat transfer coefficient was calculated to 4.9 $W/m^2 - k$

## 3.2    Presentation of cases

A comparison is to be made between reactor models run for a range of temperatures and CFD-models for two different temperatures, the cases that are going to be presented are displayed in Figure 3.7.



**Figure 3.7:** Block scheme of the models and scenarios that are run

Details of each setup are described in the sections below.

## 3.3   CSTR and PFR-model

The CSTR and PFR models were simulated in MATLAB® with an ODE-solver. Different retention times and temperatures were run to form a basis for comparison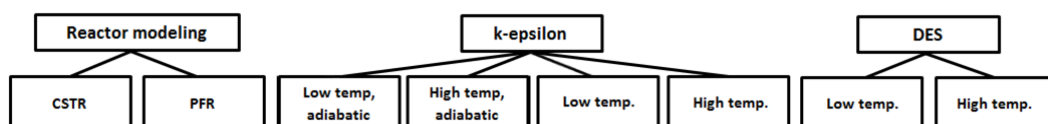, and material data was obtained from measurements at Rörvik. The reactors were adiabatic, and equimolar flow was assumed due to the excess of $N_2$ in the flue gas. The modeling of the urea spray is not included, instead $NH_3$ is introduced at the inlet in equimolar amounts in regard to NO. This very simplified simulation of the urea-SNCR process serves to make a rough comparison with the more sophisticated models.

## 3.4   k-$\epsilon$ model

The setup for the k-$\epsilon$ models are described below. The case specifics for the adiabatic scenarios and the cases with heat loss were the same except for the heat transfer coefficient, which naturally was zero for the adiabatic case.

### 3.4.1   Mesh for k-$\epsilon$ model

The mesh was made with the meshing software provided in ANSYS FLUENT. The meshing software is a unstructured grid generation program. The mesh consisted of tetrahedral cells with an inflation layer at the boundaries to provide acceptable y+ values. The size of the mesh was 75 000 cells.

### 3.4.2   Inlet, outlet and wall boundary conditions

The inlet temperature and material data were obtained from the measurement data in the procedure explained in 3.1.2 Measurement data from Rörvik. The inlet velocity profile was fully developed with respect to the inlet pipe. The fully developed flow was created by collecting data 4 diameters downstream of the inlet and inserting that data in the inlet, this process was repeated until the velocity profile for both locations were the same.

The pressure outlet boundary condition was implemented at the outlet. The wall boundary condition was no-slip with a specified heat loss constant or adiabatic depending on which case was run.

### 3.4.3   Models

The standard k-$\epsilon$ model was used together with standard wall functions. The turbulence-chemistry interactions were modeled with finite-rate/eddy dissipation. The discrete phase was modeled using unsteady particle tracking and interactions with the continuous phase were considered. The discrete random walk model was used to simulate dispersion of particles caused by turbulence.

### 3.4.4 Solution methods

The pressure velocity coupling was done by the SIMPLE scheme. For the discretization of the convective terms the second order upwind scheme was used on momentum, while first order upwind scheme was used when calculating the turbulent kinetic energy and turbulent dissipation rate.

### 3.4.5 The simulation

The simulations were run until the monitored temperature at 3 meters was stable and the scaled continuity residual was $< 10^{-4}$.

## 3.5 DES-models

Here the specifications for the DES-simulations are described.

### 3.5.1 Mesh for DES

The mesh used in the k-$\epsilon$ model was refined in order satisfy the required spatial resolution for a DES-simulation. The smallest eddies to be resolved were those with a cell length of 4cm, and it was required that there should be a couple of cell length per integral length scale to provide sufficient spatial resolution.

The refinements were made in ANSYS FLUENT by refining regions where the large eddy length scale was >4cm until the resolution was four cell lengths per smallest resolved large eddy length scale. At first only these regions were refined in order to keep down the number of cells,but this created "islands" of regions with finer mesh. Further regions were therefore refined in order to connect the isolated regions of refined mesh. A cross-section of the grid density of the resulting mesh can be viewed in Figure 3.8. After these refinements the number of cells was 2.5 million.
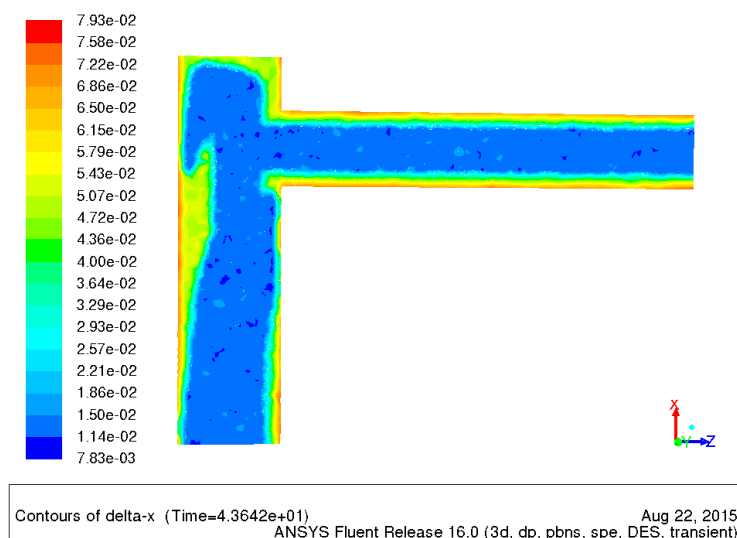


**Figure 3.8:** A crossection of the pipe displaying the cell lengths, the units are in meters.

### 3.5.2   Inlet, outlet and wall boundary conditions

Spectral perturbations was selected as inlet condition, and an instantaneous velocity field was generated from the converged k-$\epsilon$ results as the initial condition. The outlet and wall boundary conditions were the same as for the k-$\epsilon$ models.

### 3.5.3   Models

The RANS model in the DES-simulation was was SST k-$\omega$, and the Delayed DES was chosen in order to ensure that the RANS-model is used for the entire boundary layer, to reduce the risk of grid induced separation [30]. The specifications for the discrete phase were the same as for k-$\epsilon$ but with discrete random walk model disabled, in order to make the impact of resolved eddies on the spray more visible. The turbulence-chemistry interactions were modeled with finite-rate/eddy-dissipation.

### 3.5.4   Solution methods

The solution methods are: Second order implicit scheme as the transient formulation, the central differencing scheme for discretization of the convective terms, and the SIMPLE scheme for the pressure-velocity coupling.

### 3.5.5   Transient data sampling

Data sampling was enabled after the solution had reached statistical steady state which was after a simulation time corresponding to a few retention times. Data was sampled for further 8 retention times to collect reliable mean and RMS data.

# 4

# Results and discussion

The simulation results will be presented and discussed in this chapter. The focus of the discussion will be the $NO_x$ reduction calculated by the models compared to the measurement data from Rörvik. Possible explanations for the differences between simulation and measurement data is also going to be discussed.

These analyses are done to conclude which models are best at predicting the urea-SCNR process, and most useful in assisting the further development of the technique.

## 4.1 $NO_x$ reduction

The results for the $NO_x$ reduction at the three meter measuring point are shown below in Figure 4.1. Note that the models are positioned on the x-axis according to their inlet temperature.

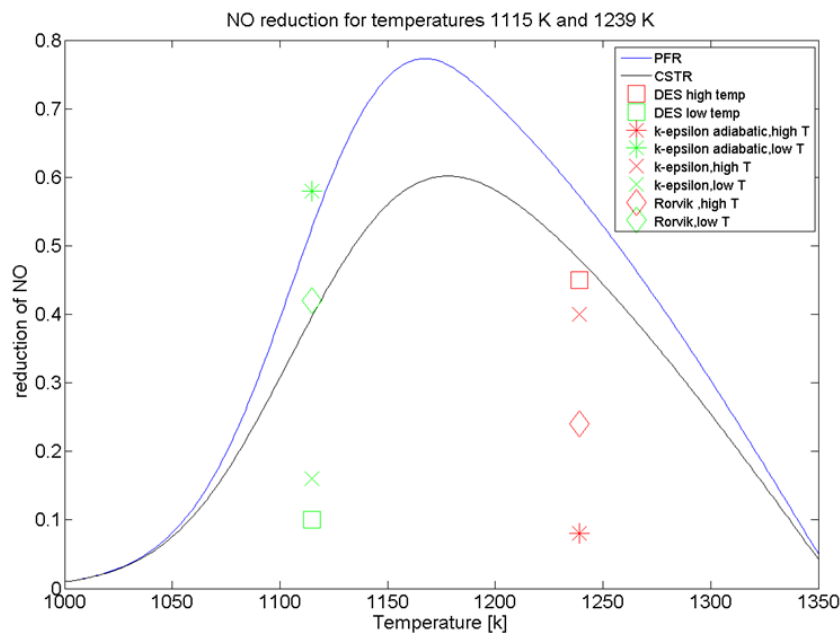

**Figure 4.1:** A graph depicting the $NO_x$ reduction for the simulated models, for the high and low operating temperatures. $NO_x$ reduction is also given for a range of temperatures for the CSTR and PFR-models

Figure 4.1 shows the following:

1. The adiabatic k-$\epsilon$ models have a higher $NO_x$ reduction compared to the measured data at the low temperature, and a lower $NO_x$ reduction compared to the measured data at the higher temperature.
2. The CSTR and PFR-models seem to be close to the measured values at the low temperature, but not so close at the high temperature.
3. At the lower temperature, the non-adiabatic k-$\epsilon$ and the DES model predicts a $NO_x$ reduction that is lower than the measurement from Rörvik. The DES model predicts the lowest NOx-conversion at this temperature.
4. At the higher temperature, the non-adiabatic k-$\epsilon$ and the DES model predicts a $NO_x$ reduction that is higher than the measurement from Rörvik. The DES model predicts the highest $NO_x$ reduction at this temperature.
5. The optimal temperature for $NO_x$ reduction is approximately at 1190K according to the reactor models, which corresponds well to literature data [6].

These results are analyzed and explained in following subsections.

### 4.1.1 The over- and underestimation of the $NO_x$ reduction by the adiabatic k-$\epsilon$ models

The overestimation of the $NO_x$ reduction at the lower inlet temperature is a consequence of the adiabaticity of the model and the optimal temperature for $NO_x$ reduction being higher than the lower inlet temperature, see Figure 4.1. Since the exhaust pipe at Rörvik experience heat losses, the mean operating temperature will be lower than the inlet and thus have a lower $NO_x$ reduction compared to an adiabatic model, which has a mean temperature closer to the inlet temperature and therefore closer to the optimal $NO_x$ reduction temperature.

The underestimation of the $NO_x$ reduction given by the adiabatic $k - \epsilon$ model at the higher temperature is explained in similar fashion: The high temperature cases are run at a temperature higher than the optimum temperature for $NO_x$ reduction, therefore cases with heat loss will have a lower mean temperature and will thus be closer to the optimum $NO_x$ reduction temperature.

Here it is concluded that the adiabatic k-$\epsilon$ models are not good at predicting the $NO_x$ reduction for this setup, since the heat losses play an important part in the modeling of this process. These models will therefore not be discussed further.

### 4.1.2 The $NO_x$ reduction of CSTR and PFR models

By just looking at Figure 4.1 the reactor models seem to predict the reduction of $NO_x$ at the low temperature quite well, where the prediction given by the CSTR-reactor model is the closest. For the higher operating temperature, the $NO_x$ reduction obtained from the reactor models are not close to the $NO_x$ reduction given by measurement data.

Although the reactor models can serve to provide a crude estimate of the $NO_x$ reduction and the optimal operating temperature, the models are not valid in this particular case. It is because there is radial variation of $NO_x$ mass fraction in the exhaust pipe, see Figures 4.2-4.5, which invalidates the assumptions made in both

reactor models. The better prediction at the lower temperature by the reactor models is most likely a coincidence.

The reactors are modeled as adiabatic, and it is possible to model heat loss in both reactors to describe the process better. Such complication of the models would however not be justified since the assumption of negligible radial gradients is violated.

Further, the models are too crude to give information that would be relevant to further improve the process, such a placement of the urea injectors. The reactor models will therefore not be investigated or discussed any further.
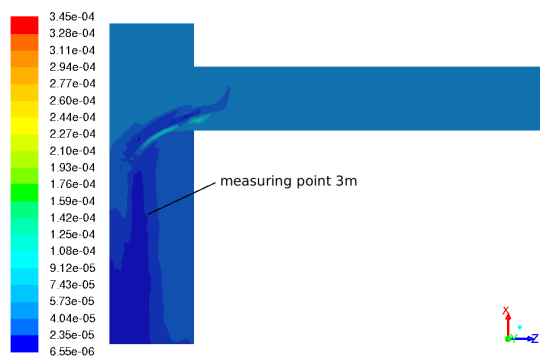


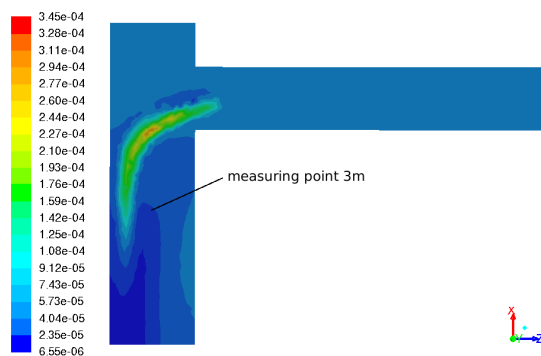**Figure 4.2:** DES high temperature, contour plot $NO_x$ mass fraction



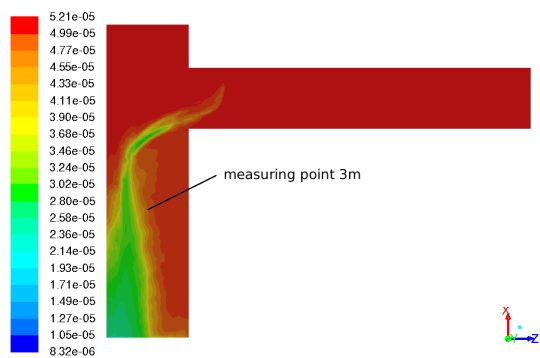**Figure 4.3:** k-$\epsilon$ high temperature, contour plot $NO_x$ mass fraction



**Figure 4.4:** DES low temperature, contour plot $NO_x$ mass fraction
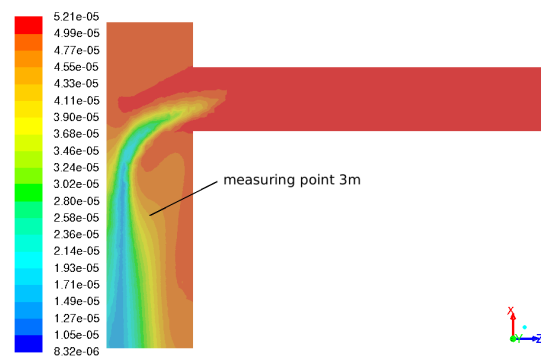


**Figure 4.5:** k-$\epsilon$ low temperature, contour plot $NO_x$ mass fraction

### 4.1.3 The over- and underestimation of the $NO_x$ reduction by the non-adiabatic k-$\epsilon$ and DES models

The non-adiabatic k-$\epsilon$ and DES models underestimation of the $NO_x$ reduction for the low temperature, and overestimation for the high temperature, could be explained by the measuring technique carried out at Rörvik, and the assumptions made regarding it. From Figures 4.2-4.5 it is seen that the mass fraction of $NO_x$ changes quite a lot in the plane perpendicular to the flow at measuring height 3 meters. If these models

are a good representation of the reality, displacing the measuring point even by small distance changes the mass fraction of $NO_x$. Further, since the mass fraction of $NO_x$ increases from left to right for the models at a higher temperature, and decreases from left to right for the models at a lower temperature, a common measuring point to the left if the middle center for all the models might move the values for $NO_x$ reduction closer to the measurements from Rörvik. As if the measurements at Rörvik were not carried out at the center of the pipe, but rather some distance to the left.

It would also be interesting to investigate the interval of possible values for $NO_x$ reduction obtained from the models at a plane situated at the measuring height of 3 meters. These points are evaluated by:

1. Searching for a point to the left of the center of the pipe that would bring the data from the models closer to the measured $NO_x$ reduction.
2. Finding max-and mean values of the $NO_x$ reduction in a plane with half the diameter of the pipe placed perpendicular to the flow at a height 3 meters. These values are then inserted into Figure 4.1 to create error bars for the values obtained in the simulations.

The aim of both evaluations are to show if data can be obtained from the k-$\epsilon$ and DES simulations that are close to the measurement data.

#### 4.1.3.1 Placement of the measuring point that brings the simulation data closest to the measurement data

The best possible match between the measured $NO_x$ reduction and the models is achieved by moving the measuring point 30 cm to the left, which corresponds to an angle of 4 deg. A plot of the resulting $NO_x$ reductions is shown below in Figure 4.6.
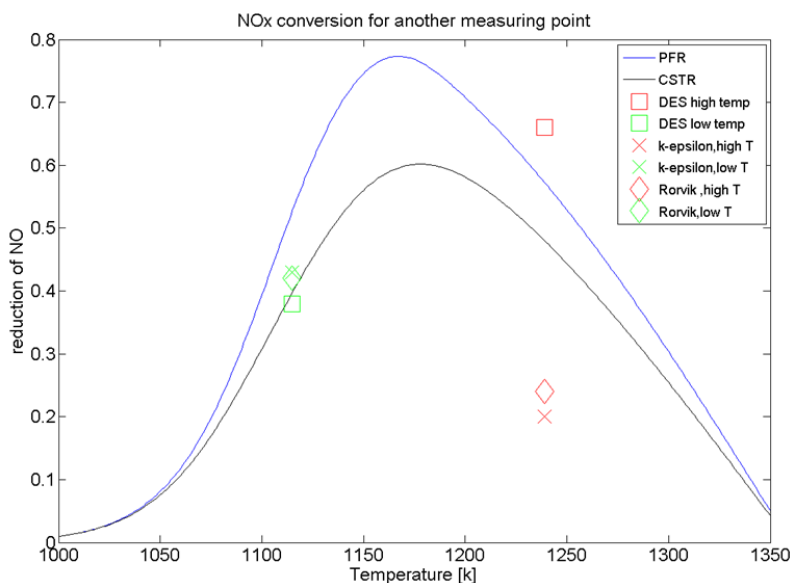


**Figure 4.6:** A graph depicting the NOx reduction for the simulated models, where the data sampling point for the models has been moved 30 cm to the left

Here the NO$_x$ reduction for the both k-epsilon cases, and the DES model for the low temperature are closer to the measured values. It was also possible to obtain NO$_x$ reduction values close to the measured data for the DES high temperature case, but this was in a region right of the measuring point where no other cases approached the measured values. The contour plots in Figure 4.2-4.5 and the analysis done here clearly shows that the concentration profile for the DES high temperature differ from the other three cases looked into here. Possible explanations of this behavior and the general differences between the DES and k-$\epsilon$ models will be will be investigated in subsection 4.1.4 Differences in predicted NO$_x$ reduction between k-$\epsilon$ and DES models.

### 4.1.3.2 The interval of possible NO$_x$ conversion values for the non-adiabatic k-$\epsilon$ and DES cases

The interval of possible NO$_x$ conversion values for the non-adiabatic k-$\epsilon$ and DES cases are shown in the plot below in Figure 4.7. The values are obtained by collecting maximum and minimum values for NO$_x$ reduction in a disc with half of the pipe diameter situated at the measuring height of 3 meters. The size of the disc was chosen based on what was considered to be a plausible location for the measurements.
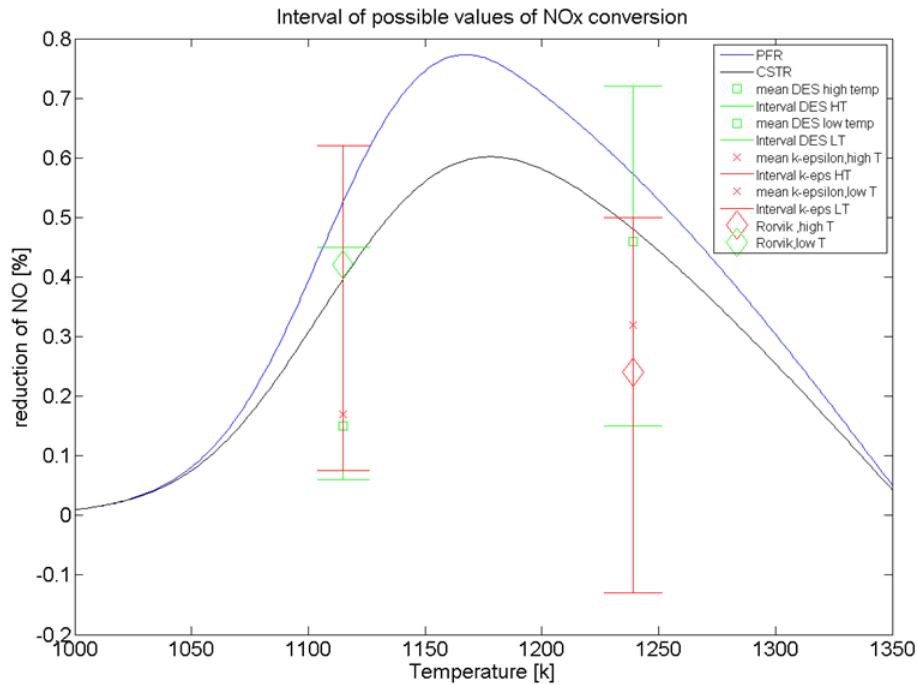


**Figure 4.7:** A graph depicting the intervals and mean values of NO$_x$ reduction for the non-adiabatic k-$\epsilon$ and DES simulations

As can be seen from the figure above, it is possible to obtain values of the NO$_x$ reduction from all the models which are equal to the measured values. It is also interesting to notice that the mean values of k-$\epsilon$ and DES at the higher temperature are further apart from each other compared to the lower temperature. This will be further investigated in subsection 4.1.4 Differences in predicted NO$_x$ reduction between k-$\epsilon$ and DES models.

Plots showing the NO$_x$ reduction in the whole plane located at the measuring height of three meters are are provided in Figures 4.8-4.11 to visualize the variation of NO$_x$ reduction values.(Note that these contour plots are taken from above, so moving the measuring point to the left in Figures 4.2-4.5 corresponds to moving the measuring point to the right in Figures 4.8-4.11. From these figures it is also evident that the contours are asymmetric over the xy-plane which divides the contours shown in two parts along the z-axis. Symmetry is expected since the spray is injected from above in the inlet pipe, which is along the xy-plane. The asymmetrical behavior is probably caused by the interaction of the computational cells and the turbulence-spray interaction, which is discussed further in subsection 4.1.5.
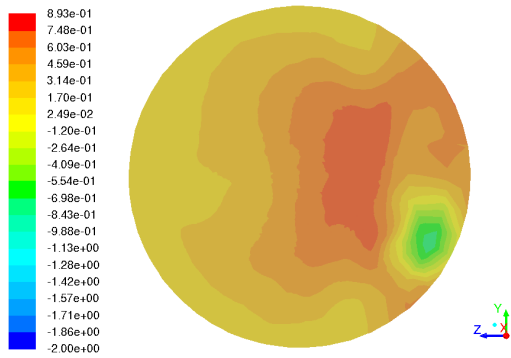


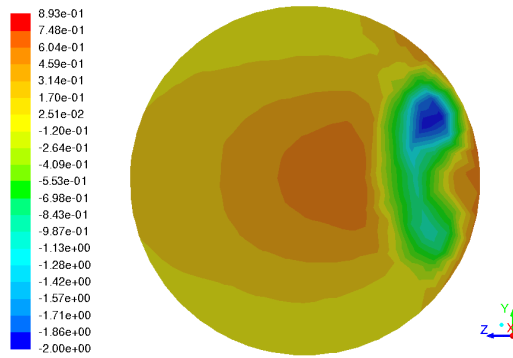**Figure 4.8:** DES high temperature, contour plot NO$_x$ reduction



**Figure 4.9:** k-$\epsilon$ high temperature, contour plot NO$_x$ reduction
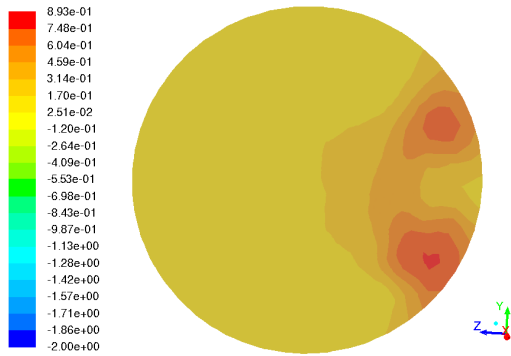


**Figure 4.10:** DES low temperature, contour plot NO$_x$ reduction
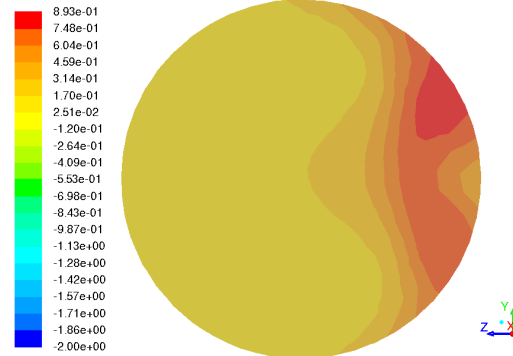


**Figure 4.11:** k-$\epsilon$ low temperature, contour plot NO$_x$ reduction

From Figure 4.6 it can be concluded that the max and min values for NO$_x$ reduction given by the k-$\epsilon$ simulations are more evenly distributed around the measurement data. Even though this is not statistically correct data, it could imply that the k-$\epsilon$ models provide a better description of the real process. More importantly, it dose not provide any evidence that the costly DES models are better at describing the process than the cheaper k-$\epsilon$ models.

There is a study showing that LES-models are better than k-$\epsilon$ models at predicting flow at pipe-bends [31], but the case was adiabatic, without chemical reactions,

and did not have a discrete phase. It is however evident that the difference in concentration fields between k-$\epsilon$ and DES models at the high temperature is prominent. This difference would be interesting to study further to see if there are any advantage of using DES for higher temperatures, perhaps not only for this case but other cases as well with other geometries or operating conditions.

To further evaluate whether the DES or k-$\epsilon$ models are best at describing the process studied in this thesis, more measurement data would be needed. The added measurements would preferably be collected at a fixed plane perpendicular to the flow to account the large radial variations in temperature and concentration. It would also be interesting to collect measuring data at a higher frequency to evaluate the fluctuating components given by the DES simulations.

### 4.1.4 Differences in predicted NO$_x$ reduction between k-$\epsilon$ and DES models

Two sources of differences between the k-$\epsilon$ and DES simulations results are going to be discussed here. They are: the impact of using a heat transfer coefficient developed for k-$\epsilon$ models on the DES models, and the difference in modeling the diffusion of temperature and concentration caused by turbulence.

#### 4.1.4.1 Differences caused by the heat transfer coefficient

The heat transfer coefficient used to describe the heat loss was calculated in the k-$\epsilon$ models. To see how well the heat transfer coefficient worked for the DES models, the temperature at measuring height at three meters obtained from the DES simulations were compared with the temperature at three meters obtained from the k-$\epsilon$ simulations.

The difference in temperature at three meters for the models was 5 K on average of the whole plane, and 20 K at a point in the center of the plane. Since the total temperature drop from inlet to the measuring height of three meters was 80 K and 90 K for the low temperature case and the high temperature case respectively, this impact was determined to be a sizable factor for the different results from the k-$\epsilon$ and DES simulations.

The difference in predicted NO$_x$ reduction between DES and k-$\epsilon$ models could be reduced by calculating a heat transfer coefficient for the DES models. That procedure would however require a lot of computational resources.

#### 4.1.4.2 Differences caused by diffusion of properties by turbulence

A big difference between the k-$\epsilon$ and DES models is the contours of the mass fraction of NO$_x$, especially for the higher temperature, seen in Figure 4.2 4.5. One characteristic that is noticeable is that the mass fraction profile appears more "smeared out" in the k-$\epsilon$ models. It is also visible that the production of NO$_x$ is more prominent in the k-$\epsilon$ model for the high temperature case, which leads to big differences in concentration profile. Both of these phenomena can be explained by how k-$\epsilon$ and DES handles the instant velocities components caused by turbulence.

As explained in the theory chapter, the k-$\epsilon$ accounts for the instant velocities components caused by turbulence by modeling them as turbulent diffusion, which is analogous to molecular diffusion. The DES model on the other hand directly solves the largest instant velocity components for each time step, and the resulting profiles are a result of taking mean values over the total number of time steps. It is therefore possible that differences in mass fraction profiles would decrease if data would be sampled over more time for the DES models, else it could be that the turbulent diffusion is overestimated in the k-$\epsilon$ models.

The big difference between the high temperature models can also be explained by this behavior. For the higher temperature, the $NO_x$ producing reaction seen in Eq. 2.2 is active and the reaction is very temperature dependent. For both of the models, the urea is introduced by the spray at 300 K. Since the k-$\epsilon$ model "smears out" the temperature and concentration over a larger volume due to the modeling of turbulent diffusion, the ammonia (which is decomposed from urea), will exhibit higher temperature and therefore more ammonia will oxidate into $NO_x$. In the DES model the ammonia and the lower temperature are not smeared out over the volume, which will lead to less ammonia being converted into $NO_x$. Even if more transient data is collected and averaged, this difference would still be visible since the temperature and ammonia will always follow the same path in the DES models, since the turbulence is modeled by convection the temperature and concentration will be tossed around by the same eddies. Why the modeled turbulent diffusion in k-$\epsilon$ is unable to compensate for this behavior that is seen in the DES models is because the $NO_x$ is dependent on many complex and un-linear phenomena such as kinetic reaction rate and mixing.

To determining which of these models are better at predicting the "reality", more measuring data would be needed.

### 4.1.5 Possible reasons for the asymmetric behavior of the $NO_x$ reduction contours plots at a plane at measuring height 3 meters

As seen in Figures 4.8-4.11, the $NO_x$ reduction profile is not symmetric in the plane located at height 3 meters, which is expected since the spray is injected symmetrically. The asymmetry is probably caused by a combination of two phenomena: the impact of the mesh on the source terms from the spray, and the nature of the flow where the urea is decomposed to ammonia.

Below in Figure 4.12 it is seen that the part of the spray which contain pure urea is asymmetric, the concentration is higher on the right side of the spray. The asymmetry of the urea concentration is in turn caused by the grid in this region of the spray. The spray is injected symmetrically but since the cells are not fine enough and not symmetric, the source terms in the transport equations originating from the modeling of the particles will be shifted from the middle because source terms are calculated in the center of these cells.
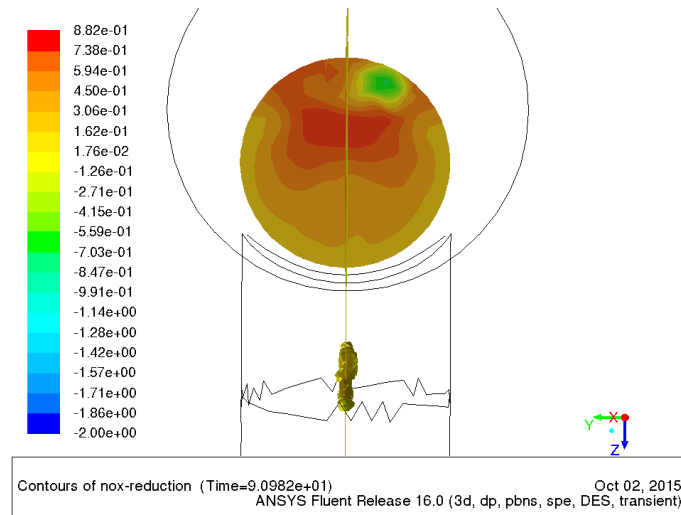
**Figure 4.12:** An iso-surface of the mean DPM concentration of urea for the DES high temperature case, also the plane at height 3 meters is also visible in the figure. The contours are displaying the NO$_\text{x}$ reduction.

The region where the spray consist of pure urea is naturally the region where the urea will be decomposed into ammonia. In this region the flow field has two rotational centers due to the pipe bend, as explained in [32], which will split the ammonia concentrations into two swathes. This behavior of the flow will increase the asymmetry caused by the cells in the spray region and lead to asymmetry in ammonia concentrations, which in turn will lead to an asymmetric NO$_\text{x}$ reduction profile at measuring height 3 meters. These swathes of ammonia are displayed below in Figure 4.13.
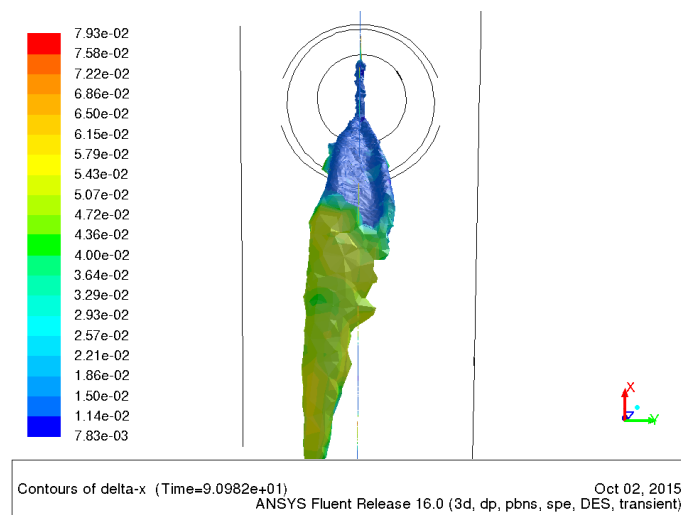


**Figure 4.13:** An iso-surface of the mean DPM concentration of urea and iso-surface for a ammonia concentration for the DES high temperature case. The contours are displaying the cell length.

In Figure 4.13 it is apparent that the swath in the negative y-direction (corresponding to right in Figure 4.12) is much larger, therefore there will be a higher

concentration of ammonia on this side of the symmetry line. It is also noticeable that when the swathes moves into a region with larger cells (green and yellow color in Figure 4.13) the asymmetry is enhanced - the smaller swath visualized with an iso-surface for a particular ammonia concentration disappears.

Here the asymmetry of the DES high temperature case was investigated but the asymmetry for the other cases was caused by the same mechanisms.

Ways to decrease the asymmetry would be refine the grid at the spray. If the asymmetry is mainly caused by the flow field in the DES simulations, further sampling time would make the flow more symmetric. Since the asymmetry probably is caused a combination of the grid and the rotational centers, both refining the grid at the spray and increasing the sampling time would probably lead to a more symmetric $NO_x$ reduction profile.

# 5
# Conclusions

- The heat loss is an important factor to consider when modeling the urea SNCR process.

- Even though there is literature supporting that LES models are better than k-$\epsilon$ models at predicting the flow in pipe-bends [31], the added complexity caused by having chemical reactions, heat losses and a dispersed phase described in the model has not been observed to give any obvious advantages of using DES. It is however observed that there are large differences in $NO_x$ reduction for the higher operating temperature between DES and k-$\epsilon$, so there could be some effects that the DES model describes better, but this would require further investigation.

- Since there was no indication that the DES-model was better at describing the process than the k-$\epsilon$ model, the computationally cheaper k-$\epsilon$ model is regarded as sufficient for optimization for this process.

- More measurements are needed to determine if using a DES-model could be better at describing the process, preferably along fixed planes perpendicular to the flow since there are big radial variations in temperature and concentration, and/or a higher frequency of the measurements to allow for a comparison of the fluctuating components.

- The asymmetric behavior of the $NO_x$ reduction obtained in the k-$\epsilon$ and DES simulations could be decreased by refining the mesh near the spray and increasing the sample time of unsteady data for the DES cases.

# 5. Conclusions

# Bibliography

[1] B. Farcy, A. Abou-Taouk, L. Vervisch, P. Domingo and N. Perret, "Two approaches of chemistry downsizing for simulating Selective Non Catalytic Reduction DeNOx Process", vol. 118, pp. 291-299, 2014.

[2] M. Kampa and E. Castanas, "Human health effects of air pollution", Enviromental Pollution, vol. 151, pp. 362-367, 2008.

[3] D. L. Mauzerall, B. Sultan, N. Kim and D. F. Bradford, "NOx emissions from large point sources: variability in ozone production, resulting health damages and economic costs", Atmospheric Environment, vol. 39, no. 16, pp. 2851-2866, 2005.

[4] Mahmoudi, Shiva, Baeyens, Jan, Seville and J. P. K., "NOx formation and selective non-catalytic reduction (SNCR) in a fluidized bed combustor of biomass", Biomass and Bioenergy, vol. 34, no. 9, pp. 1393-1409, 2010.

[5] Salzmann R. "Fuel Staging for NOx reduction in Biomass Combustion: Experiments and Modeling", Energy and Fuels, no. 15, pp. 575-582, 2001.

[6] B. v. d. Heide, "SNCR Process - Best Available Technology for NOx Reduction in Waste to Energy Plants", Mehldau & Steinfath Umwelttechnik, Presented at POWER-GEN Europe Milan, 3-5 June 2008.

[7] P. Schaber, J. Colson, S. Higgins, D. Thielen, B. Anspach, J. Brauer, "Thermal decomposition (pyrolysis) of urea in an open reaction vessel", Thermochimica Acta, vol. 424, no 1-2, pp. 131–142, 2005.

[8] R. Rota, D. Antos, E. F. Zanoelo, M. Morbidelli, "Experimental and Modeling Analysis of the NOxOUT Process", Chemical Engineering Science, vol 57, pp. 27-38, 2002.

[9] M. Ostberg, K. Dam-Johansen, "Empirical Modeling of the Selective Non-Catalytic Reduction of NO: Comparison with Large-Scale Experiments and Detailed Kinetic Modeling", Chemical Engineering Science, vol 49, no.12, pp. 1897-1904, 1994.

[10] J. Brouwer, M. P. Heap, D. W. Pershing, P. J. Smith, "A Model for Prediction of Selective Non-Catalytic Reduction of Nitrogen Oxides by Ammonia, Urea, and Cyanuric Acid with Mixing Limitations in the Presence of CO", In 26th Symposium on Combustion, The Combustion Institute, 1996.

[11] G. W. Roberts, "Chemical Reactions and Chemical Reactors", 1st edition, 2009.

[12] B. Andersson, R. Andersson, L. Håkansson, M. Mortensen, R. Sudiyo, B. van Wachem. "Computational Fluid Dynamics for Engineers", 11th edition, 2015.

[13] D. C. Wilcox, "Reassessment of the scale-determining equation", AIAA journal, vol. 26, no. 11, 1988.

[14] D. C. Wilcox, "Turbulence Modeling for CFD", DCW Industries, Inc., La Canada, California 91011, 1998.

[15] ANSYS® Academic Research, Release 16.0, Help System, Fluent Theory guide, Standard 4.4.1. k-omega model, ANSYS, Inc.

[16] ANSYS® Academic Research, Release 16.0, Help System, Fluent Theory guide, 4.14.7. y+-Insensitive Wall Treatment $\omega$-Equation, ANSYS, Inc.

[17] F. R. Menter, "Zonal Two Equation k-omega Turbulence Models for Aerodynamic Flows", AIAA Paper 93-2906, 1993.

[18] J. Smagorinsky, "General circulation experiments with the primitive equations", Monthly weather review, vol.91, no. 3, 1963.

[19] F Nicoud, F Ducros, "Subgrid-scale modelling based on the square of the velocity gradient tensor," Flow, turbulence and combustion, vol. 63, pp.183-2000, 1999.

[20] H. K. Versteeg, W. Malalsekera, "An introduction to Computational Fluid Dynamics - The Finite Volume Method", 2:nd edition, 2007.

[21] R. Kraichnan, "Diffusion by a Random Velocity Field", Physics of Fluids, vol. 13 pp. 21-31, 1970.

[22] R. Smirnov, S. Shi, and I. Celik, "Random Flow Generation Technique for Large Eddy Simulations and Particle-Dynamics Modeling", Journal of Fluids Engineering, vol. 123, pp. 359-371, 2001.

[23] F. R. Menter, M. Kuntz, and R. Langtry. "Ten Years of Experience with the SST Turbulence Model", Heat and Mass Transfer, vol.4, Begel House Inc., pp.625-632, 2003.

[24] ANSYS® Academic Research, Release 16.0, Help System, Fluent Theory guide, 4.11.4. DES with the BSL or SST k-omega Model, ANSYS, Inc.

[25] B. F. Magnussen and B. H. Hjertager, "On mathematical models of turbulent combustion with special emphasis on soot formation and combustion", In 16th Symp. (Int'l.) on Combustion, The Combustion Institute, 1976.

[26] S. A. Morsi and A. J. Alexander. "An Investigation of Particle Trajectories in Two-Phase Flow Systems". J. Fluid Mech. vol. 55 no. 2, pp.193–208, 1972.

[27] H. Ström, A. Lundström, B. Andersson, "Choice of urea-spray models in CFD simulations of urea-SCR systems", Chemical Engineering Journal, vol. 150, pp.69-82, 2009.

[28] ANSYS® Academic Research, Release 16.0, Help System, Fluent Theory guide, 16.2.1. Equations of Motion for Particles, ANSYS, Inc.

[29] A Lundström, B Waldheim, H Ström, and B Westerberg, "Modelling of urea gas phase thermolysis and theoretical details on urea evaporation", Journal of Automobile Engineering, vol. 255, pp. 1392-1398, 2011.

[30] M. S. Gritskevich, A. V. Garbaruk, J. Schütze, F. R. Menter, "Development of DDES and IDDES Formulations for the k-$\omega$ Shear Stress Transport Model", Flow Turbulence Combustion, vol. 88, pp.431-449, 2011.

[31] R. Röhrig, S. Jakirlic, C. Tropea, "Comparative computational study of turbulent flow in a $90^o$ pipe elbow", International Journal of Heat and Fluid Flow, doi:10.1016/j.ijheatfluidflow.2015.07.011, 2015.

[32] H. Ström, S. Sasic, B. Andersson, "Design of automotive flow-through catalysts with optimized soot trapping capability", Chemical Engineering Journal, vol. 165, no. 9 pp.934-945, 2010.